Title

Large-scale efficient mid-wave infrared optoelectronics based on black phosphorus ink.

Journal

Science Advances, 9(49)

Authors

Gupta, Niharika

Wang, Shu

Higashitarumizu, Naoki

et al.

Publication Date

2023-12-08

DOI

10.1126/sciadv.adi9384

Peer reviewed

PHYSICAL SCIENCES

Large-scale efficient mid-wave infrared optoelectronics based on black phosphorus ink

Niharika Gupta[1,2], Shu Wang[2,3], Naoki Higashitarumizu[1,2], Vivian Wang[1,2], Kyuho Lee[1,2,4], Cheolmin Park[4], Ali Javey[1,2]*

The mid-wave infrared (MWIR), ranging from 2 to 5 micrometers, is of substantial interest for chemical sensing, imaging, and spectroscopy. Black phosphorus (bP)–based MWIR light emitters and detectors have been shown to outperform the state-of-the-art for commercial devices due to the low Auger recombination coefficient of bP. However, the scalability of these devices remains a challenge. Here, we report a bP ink formula that preserves the exceptional MWIR optoelectronic properties of bP to deposit centimeter-scale, uniform, and pinhole free films with a photoluminescence quantum yield higher than competing III-V and II-VI semiconductors with similar bandgaps at high excitation regime. As a proof of concept, we use bP ink as a "phosphor" on a red commercial light-emitting diode to demonstrate bright MWIR light emission. We also show that these films can be integrated into heterostructure device architectures with electron and hole selective contacts for direct-injected light emission and detection in MWIR.

INTRODUCTION

Black phosphorus (bP), the most stable allotrope of phosphorus, is promising for numerous electronics and photonics due to its unique properties. For example, the high carrier mobility and high hole saturation velocity in bP have enabled the realization of bP-based high-speed field-effect transistors (*1*). In addition, bP has a direct bandgap, which can be tuned between 0.3 and 2 eV depending on its thickness (*2*). The bandgap of bP in the bulk form, 0.3 eV, allows for room temperature operation of bP photodetectors in the mid-wave infrared (MWIR). Furthermore, bP photoconductors have been shown to have a specific detectivity higher than the commercially available MWIR detectors (*3*, *4*). The bP photodetectors also bring polarization sensitivity without external optics because of the anisotropic crystal structure of bP (*5*). Furthermore, the bandgap of bP shows strong strain tunability that can be used for actively variable-spectrum optoelectronics in the MWIR (*6*). BP light-emitting diodes (LEDs) have also been shown to have outstanding efficiencies compared to state-of-the-art MWIR LEDs based on III-V and II-VI semiconductors (*7*). This superior performance is primarily driven by the low Auger recombination coefficient in bP, which results in higher photoluminescence (PL) quantum yield than the traditional compound semiconductors of similar bandgap (*2*, *8*, *9*). However, most of the prior work on bP-LEDs and photodetectors are based on small-size, mechanically exfoliated flakes, with a lateral dimension of less than 100 μm. This is because large-scale deposition of highly crystalline bP thin films with high quantum yield is challenging.

As an alternative to the most used method of mechanical exfoliation, previous studies have also explored liquid-phase exfoliation techniques to produce bP flakes (*10*), but, because of poor dispersibility of bP in most solvents or/and high boiling point of the solvents, the solution containing bP does not culminate in large-scale uniform films with drop casting or spin casting, resulting in the device area again being limited by the size of the bP flake, as in the case of mechanical exfoliation. Other works have shown large-scale bP-based solar cells but require the addition of another key component of the active layer to the solution, reducing the applicability of the solution (*11*, *12*). The development of two-dimensional (2D) "inks" in the recent years has enabled scalable approaches to deposit 2D materials (*13*). Their formulation consists of a solvent, binder, surfactants, and other additives apart from the material itself. Considering the relevance of these materials for electronics and photonics, some of these 2D inks are now commercially available products such as graphene inks for screen printing and MoS_2 ink for spin and spray coating. The use of bP ink for inkjet printing has also been explored (*14*, *15*). However, the focus of previous works has been transistor applications, and realization of large-scale efficient MWIR optoelectronics has not yet been attempted.

In this work, we show a formulation of bP ink, which can be either spin-coated or dip pen–printed onto a desired substrate for MWIR applications, as represented in Fig. 1A. The enabled films are formed with tunable user-defined thickness (~1.5 to 10 μm), consisting of stacked small flakes that are 5- to 150-nm thick with a lateral area of less than 1.5 μm^2. This bP ink film has no pinhole in millimeter scale if it is thicker than 1.5 μm, so that the vertical heterostructure device can operate well without a current leakage. Thin films deposited using this optimized bP ink produce bright PL with a high quantum yield (~0.9%, internal) in MWIR. As a proof of concept, we show that this ink can be used as a "phosphor" on commercial red LEDs to produce bright MWIR emission. In addition, large-scale heterojunction devices based on bP films with selective electron/hole contacts are demonstrated for MWIR emission with peak intensity at ~0.3 eV, corresponding to the bandgap of bP. Last, we show that bP heterojunction devices can be configured in a reverse-bias condition as MWIR photodetectors at room temperature.

[1]Department of Electrical Engineering and Computer Sciences, University of California, Berkeley, CA 94720, USA. [2]Materials Sciences Division, Lawrence Berkeley National Laboratory, Berkeley, CA 94720, USA. [3]Department of Materials Science and Engineering, University of California, Berkeley, CA 94720, USA. [4]Department of Materials Science and Engineering, Yonsei University, 50 Yonsei-ro, Seodaemun-gu, Seoul 03722, Republic of Korea.
*Corresponding author. Email: ajavey@berkeley.edu

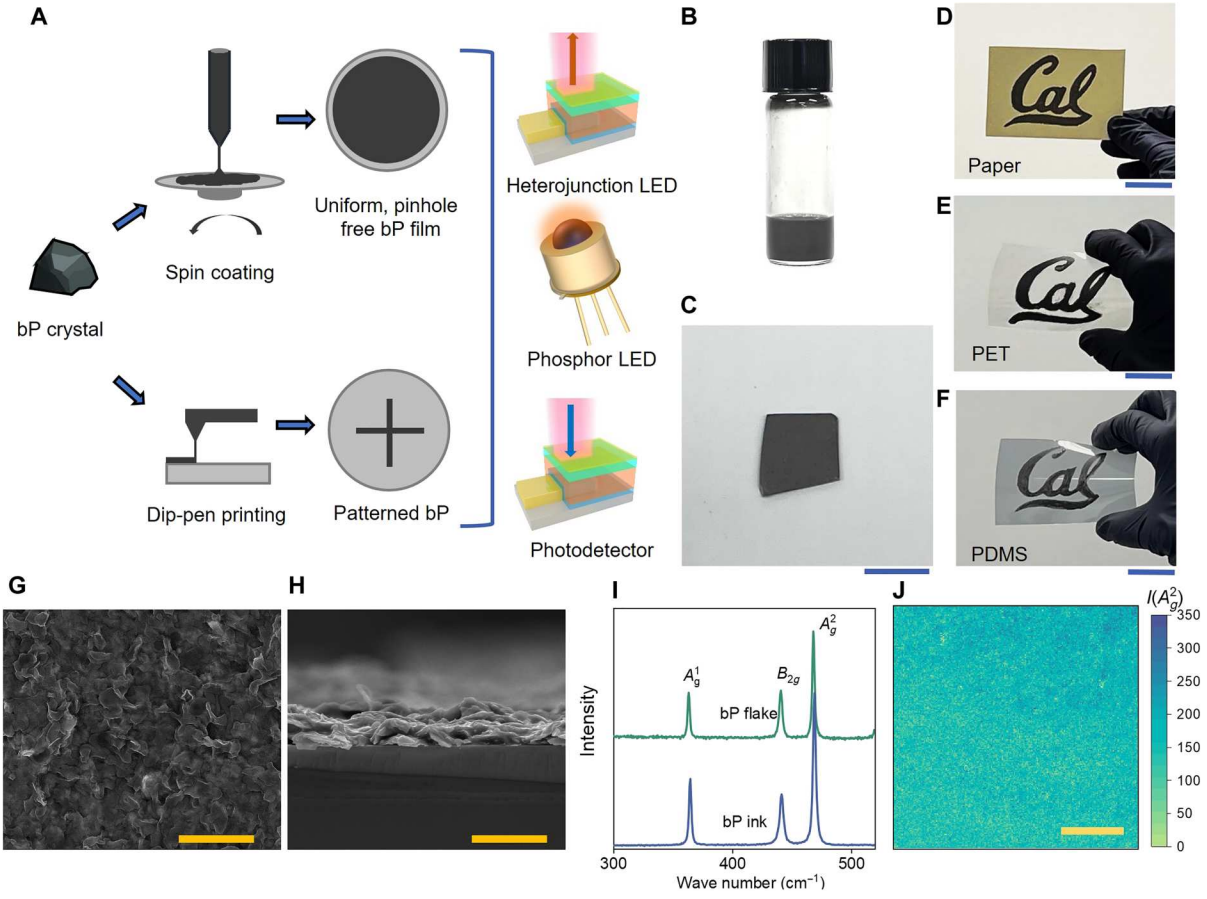

Fig. 1. Material characterization and applications of bP ink. (**A**) Schematic showing deposition techniques and applications of bP ink. (**B**) Photograph of bP ink. (**C**) Image of bP film made using spin coating of the bP ink on a ~ 5 mm–by–5 mm quartz substrate. Scale bar, 5 mm. Image of "Cal" calligraphed with dip pen on (**D**) paper, (**E**) polyethylene terephthalate (PET), and (**F**) polydimethylsiloxane (PDMS). Scale bars, 25 mm. (**G**) Top-view of SEM image of bP film on 50 nm SiO_2/Si. Scale bar, 10 μm. (**H**) Cross-sectional view of SEM image of bP film on 50 nm SiO_2/Si. Scale bar, 10 μm. (**I**) Raman spectrum for exfoliated 50-nm bP and bP ink. (**J**) Raman map of intensities at 468 cm^{-1}, $I(A_g^2)$ with 5-μm spatial step on a ~1 mm–by–1 mm area of bP film. Scale bar, 250 μm.

RESULTS AND DISCUSSION

The first step of the formulation process of the ink is to crush bulk bP crystals (Smart Elements) into powder form in a mortar and pestle. The powder was then added to *N*-methyl-2-pyrrolidone (NMP) in a vial that was ultrasonicated to further reduce the size of the bP particles. The particle size of the ink is important. Specifically, if the particles are too small, then the bandgap is increased, which is no longer of interest for MWIR applications. On the other hand, if the particles are too large, then the bP particles accumulate on the bottom and the resulting film is nonuniform. In this regard, bP particle thickness ranging from 5 to 150 nm and flake lateral area of less than 1.5 μm^2 was found to be optimal (supporting information S1). NMP, a commonly used solvent for liquid exfoliation of 2D materials, was chosen as the solvent due to its suitable Hansen solubility parameters and surface tension for dispersing and stabilizing 2D materials (*16*). The solution of bP in NMP cannot be spin-coated at room temperature because of the high boiling point of NMP of 202°C. Therefore, after the sonication, NMP was separated from the solution by centrifugation; the precipitate containing the bP particles was redispersed in toluene; and a small amount of binder, oleyl amine, was added. Oleyl amine, a commonly used capping agent in studies related to nanomaterials and quantum dot research, enhances the stability of bP particles in the solution and modifies ink viscosity and surface tension properties to aid uniform film deposition with spin-coating and drop-casting methods (*17*). Toluene dissolves oleyl amine, and its high vapor pressure facilitates faster drying during spin coating. Excess binder in the solution was washed with another centrifugation step, and the remaining material was redispersed in toluene and lastly spin-coated on a quartz substrate sized ~5 mm by 5 mm. More details on the formulation and spin-coating process are discussed in Materials and Methods. Images of the ink in a vial and an example film on a quartz substrate are shown in Fig. 1 (B and C), respectively. The thickness of these films can be varied depending on the loading of the bP in the ink (supporting information S3). The ink can be also printed with a dip pen directly on any substrate such as paper or flexible plastics like polyethylene terephthalate and polydimethylsiloxane, as shown in Fig. 1 (D to F).

Top-view and cross-sectional view images of the film obtained with a scanning electron microscope (SEM) are shown in Fig. 1 (G and H), respectively, which provide a magnified view of the film microstructure at the micrometer level. The large-scale dark-field microscope and SEM images of the bP film are included in supporting information S4 and suggest full coverage of bP particles

on a millimeter scale, with no coffee-ring effects or pinholes visible. Comparison of the Raman spectra in Fig. 1I demonstrates that the crystal structure of the bP in the ink is intact and matches that of a mechanically exfoliated ~50-nm bP flake, showing typical bP characteristics peaks at 363, 441, and 468 cm^{-1}, attributed to the A_g^1, B_{2g}, and A_g^2 phonon modes in bulk bP. The comparison of the film was done with a thicker bP flake because the film consists of bulk-bP–sized particles, and the Raman peak positions and relative intensities depend on the number of layers in the bP flake (*18*). Raster scanning was performed on the bP film to generate a Raman intensity map at the 468 cm^{-1} peak $I(A_g^2)$ for a 1 mm–by–1 mm area with a step size of 5 μm, illustrated in Fig. 1J.

Normalized spectrally resolved PL of the bP film also matches that of the exfoliated ~50-nm bP flake, whose bandgap is ~0.3 eV and the full width half maximum is ~520 nm, as depicted in Fig. 2A. This corroborates our hypothesis that the bP flakes in the ink are thick enough to be considered bulk (more than 10 layers). If they were thinner, then the PL peak would occur at a greater energy (shorter wavelength). This hypothesis is consistent with the Raman spectra of Fig. 1I. These spectra were collected using a double-modulated lock-in detection technique, as described in Materials and Methods. The spectra were obtained at different pump powers, enabling the internal PL quantum yield of the bP film to be found as a function of generation rate (Fig. 2B). The internal PL quantum yield (η_{QY}) of the film is defined as the ratio of the

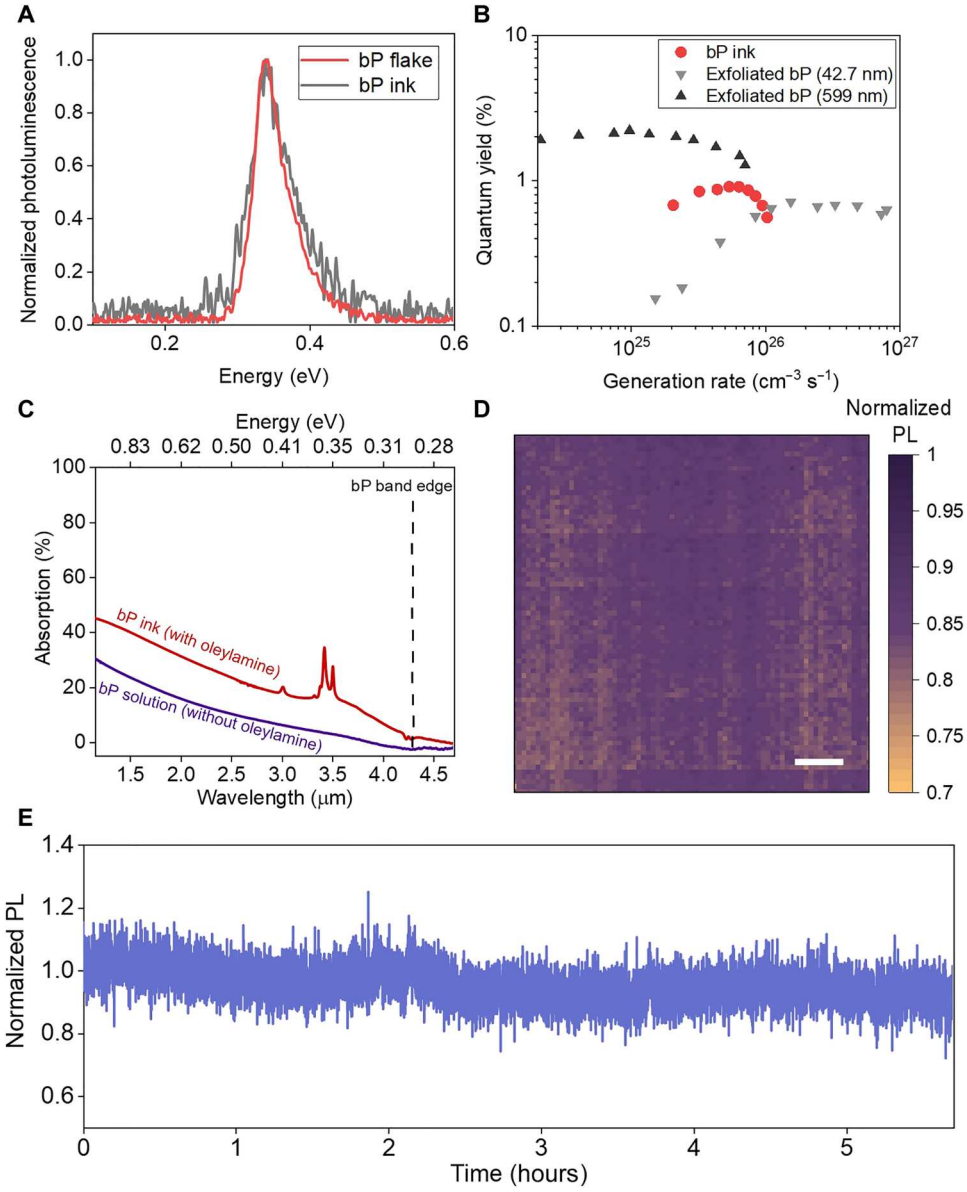

Fig. 2. bP ink PL properties. (**A**) Normalized spectrally resolved PL of bP flake and bP ink. (**B**) Internal PL quantum yield of bP ink film as a function of generation rate, compared with internal PL quantum yield for exfoliated bP flakes from (*9*). (**C**) MWIR absorption of bP ink with and without oleyl amine. (**D**) PL intensity map measured on an area of ~3.7 mm by 3.7 mm with a step size of 50 μm. Scale bar, 500 μm. (**E**) Drift measurement of PL for ~5.5 hours at a pump power of 9 mW in air.

number of photons emitted to the number of carriers generated in the film

$$\eta_{QY} = \frac{\text{number of photons emitted}}{\text{number of carriers generated}} \quad (1)$$

The PL quantum yield can be calculated according to the *ABC* model shown in the following equation

$$\eta_{QY} = \frac{B(np - n_i^2)}{A\frac{(np-n_i^2)}{p} + B(np - n_i^2) + 2Cn(np - n_i^2)} \quad (2)$$

where A, B, and C are the Shockley-Read-Hall, radiative bimolecular, and Auger recombination coefficients, respectively; and n_i and n (p) are the intrinsic and total electron (hole) concentrations, respectively. In Fig. 2B, the measured η_{QY} of the bP film is shown in contrast to the η_{QY} of exfoliated bP, calculated using Eq. 2 and data reported in previous studies (*9*). The efficiency of bP film is found to be higher than the compound semiconductors at higher generation rates because of its property of lower Auger recombination coefficient (*6*, *8*, *9*, *19*–*23*). The η_{QY} of the film increases from ~0.68 to 0.91% at low carrier concentration of 1–5 × 10^{25} cm^{-3}. At higher carrier concentration, η_{QY} decreased due to Auger recombination (*24*). The peak η_{QY} of bP film is lower to that of a exfoliated bP flake (600 nm thick, η_{QY} ~ 2%), which is attributed to bP oxidation and induced defects during ink formulation process (*9*). The PL spectrum is independent on the polarization angle and the PL intensity is constant within the measurement error, as shown in fig. S5. The reflection and the transmission profiles in the MWIR region at 10 different spots on the bP film are included in supporting information S6. The reproducible spectra at different spots prove film uniformity and negligible spot-to-spot variation. The absorbance of the bP film, calculated from the averaged reflection and transmission, is shown in Fig. 2C. It can be deduced from this figure that bP ink film absorbs wavelengths longer than ~4.2 μm (0.29 eV), which is the band edge of bulk bP and a property of thick bP flake (*5*). As evidence of the presence of a minor quantity of oleyl amine in the film, its characteristic absorption peaks at ~3 μm (3231 cm^{-1}), ~3.4 μm (2927 cm^{-1}), and ~3.5 μm (2850 cm^{-1}) are observable in these data (*25*). The absorption profile of bP solution without oleyl amine is also presented for comparison to find no signature of oleyl amine peaks. To investigate the PL uniformity, the sample was raster-scanned over an area of ~3.7 mm by 3.7 mm with a step size of 50 μm. The integrated PL (total counts of the spectrum) at each of those spots was normalized such that 0 and 1 indicate zero (no PL) and maximum signal (of all the data points), respectively. These data are illustrated in Fig. 2D, substantiating film uniformity over a large scale. Because bP is air-sensitive, the PL of bP ink film was checked for several hours to examine the drift in air (Fig. 2E).

Because the bP ink has high emitting efficiency, it was used as a MWIR phosphor on a red commercial LED that has electroluminescence (EL) peak energy higher than bP bandgap and can serve as a pump to the bP film, schematically shown in Fig. 3A. To illustrate this concept, bP was drop-casted on millimeter-sized LEDs emitting at a peak wavelength of 660 nm, as presented in Fig. 3B. The EL spectrum is shown in Fig. 3C, which is consistent with the PL spectrum (Fig. 2A). The EL spectra were collected using a similar lock-in detection technique to the PL spectrum, as described in Materials and Methods. The spectrum intensity increases as more current is injected into the device, with an external quantum efficiency (η_{EQE}) of ~0.27%. η_{EQE} is defined as the ratio between the number of detected photons and the number of electrons injected into the device

$$\eta_{EQE} = \frac{\text{number of detected photons}}{\text{number of injected electrons}} = \frac{P/(hc/\lambda)}{I/q} \quad (3)$$

Here, h is Planck's constant, c is the speed of light, P is total detected optical power, I is the injected current, and λ is the wavelength of the emitted photons. The total power output from this integrated bP ink/LED device was also analyzed as a function of the input power and is plotted in Fig. 3D. When excited with a high power laser instead of LED, the PL quantum efficiency monotonically increase up to the generation rate of 6 × 10^{25} cm^{-3} s^{-1} (Fig. 2B), although it turn to decrease at even higher generation rate due to the Auger recombination. Thus, the output power of bP-phosphor LED could saturate at such a high excitation regime.

To make large-scale efficient heterostructure LEDs based on charge injection, we used an electron transport layer (ETL) and a hole transport layer (HTL) along with the anode and cathode, a concept common in organic LEDs and quantum dot LEDs (QD-LEDs) (*26*). We have demonstrated proof of concept of MWIR large-scale bP-LEDs by spin coating large areas with poly(3,4-ethylenedioxythiophene) polystyrene sulfonate (PEDOT:PSS) and zinc oxide (ZnO) selected as HTL and ETL, respectively. This is in stark contrast to the design structure conventionally used for bP-LEDs constituting of vertically stacked heterojunction with the electron injection layer of mechanically exfoliated MoS_2 or WS_2, whose active area was limited to a micrometer scale. For the hole (bottom) and electron (top) contact, Au and indium tin oxide (ITO) were chosen, respectively. A thin film of ITO was used as the top electrode due to its optical transparency in the bP emission region. The schematic representation of the LED structure is shown in Fig. 4A, and the energy band diagram in Fig. 4B is represented using energy levels documented in previous studies (*26*–*28*). Detailed device fabrication procedure and SEM cross-sectional images are included in Materials and Methods and supporting information S7, respectively. An image of a typical chip with devices is shown in Fig. 4C, where the three gold lines are the bottom hole contacts for three different devices. The emitting device area is ~1 mm by 1 mm, where the Au lines overlap with bP film and visible to the naked eye, unlike a typical bP-LED that has an emitting area less than 1000 μm^2. Figure 4D shows typical current-voltage (I-V) characteristics exhibited by one of these devices. The LED produces EL when forward-biased, with increasing output intensity as the injected current density is increased, as shown in Fig. 4E. The variation of η_{EQE} from device to device was found to be low and ranged between 0.02 and 0.05%. These efficiencies of the champion device and the bP ink–phosphor LED are benchmarked against the state-of-the-art QD-LEDs emitting in the bP energy range, based on materials such as Pb-CdS, InAs-ZnSe, Pd, PbSe, and HgTe (*29*–*39*). As shown in Fig. 4F, these LEDs have efficiencies comparable to the QD-LEDs with similar design and peak emission region. Admittedly, the efficiency is lower compared to the state-of-the-art QD-LED, but given the high roughness of the bP film, the light outcoupling efficiency is one of the constraining factors, apart from the optimization of the device structural design. The internal quantum efficiency (η_{IQE}) of this charge-injection device, which is the number of internally generated photons, is determined to be ~0.9% by accounting for losses in light outcoupling using optical simulations discussed in

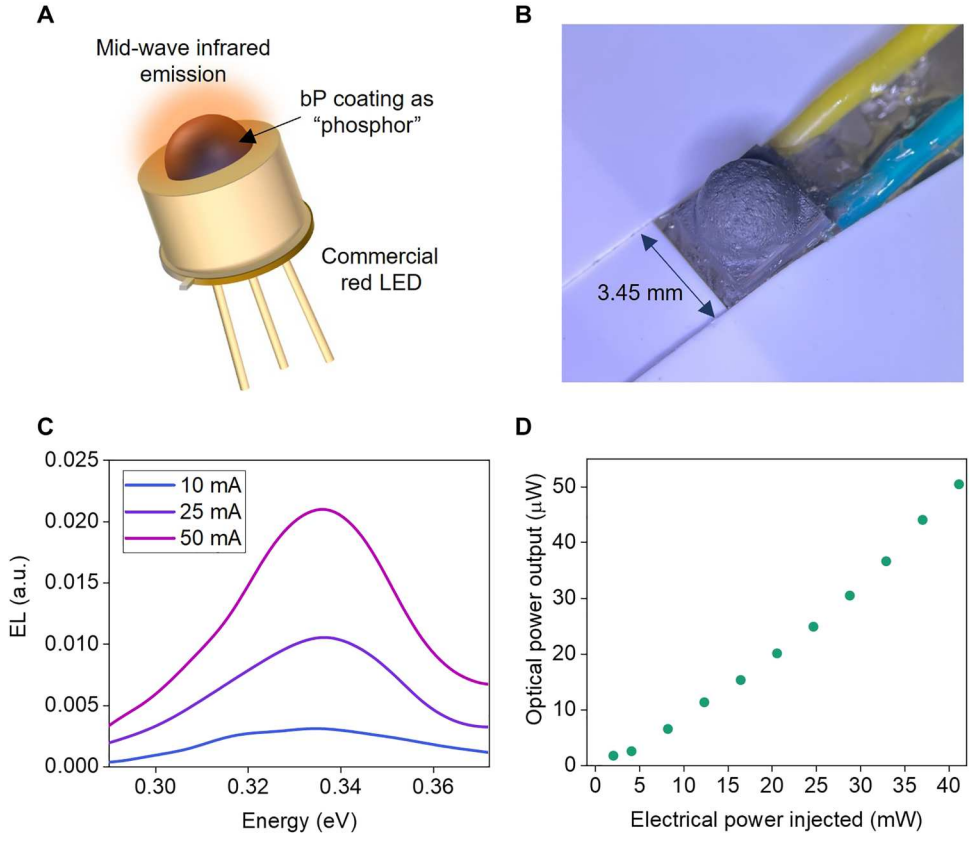

Fig. 3. bP ink as MWIR phosphor. (**A**) Schematic of bP as phosphor on red LED. (**B**) Image of bP ink film as a phosphor on a commercial-red LED. (**C**) Electroluminescence (EL) from the bP-LED shown in (B) at injected currents 10, 25, and 50 mA at the bP emission peak of ~0.33 eV. a.u., arbitrary units. (**D**) Optical power output from the bP-LED as a function of total electrical power injected.

supporting information S8, along with the experimental results

$$\eta_{IQE} = \frac{\text{number of total photons}}{\text{number of injected electrons}} \quad (4)$$

Because of the light-absorbing properties of bP film, the device shown in Fig. 4A for LED application can also be used as a photodetector but in reverse-bias configuration. This is validated from the spectrally resolved photoresponse of the device at different reverse bias conditions, shown in Fig. 5B. The peak MWIR photoresponsivity of the device is found to be 22 and 47 mA/W at a reverse bias of 2.5 and 5 V, respectively. The responsivity monotonically increased as the applied reverse bias (Fig. 5C). The photoresponsivity as a function of incident light intensity (η = 638 nm) was examined at reverse biases of 1, 3, and 5 V, as shown in Fig. 5D. The responsivity decreased as the incident light intensity increase, which corroborated that the higher light power results in lower photoresponsivity attributed to electron-trap saturation and increase in nonradiative recombination. Here, note that the film thickness was optimized to 1.5 to 10 μm to prevent the pinholes that is critical for the vertical structure, although further process optimization will be desired to achieve the film thickness of several tens to hundred nanometers optimal for the detector performance suppressing the dark current. The details on photodetector-related measurements are discussed in Materials and Methods.

In conclusion, we have demonstrated a formulation of bP ink that can be dip pen–printed or spin-coated. We show that these films match the high optoelectronic performance attributes of a bP flake while also offering a substantial advantage of scalability. We fabricate multiple device structures to demonstrate the optoelectronic properties of this large-area bP film including a bP-phosphor LED as well as a MWIR direct light emitter based on the integration of bP ink with carrier transport layers. Moreover, we present photodetectors based on these bP inks that show high responsivity to infrared light due to the high absorption of these films. For future work, other ETLs or HTLs that will further improve the LED efficiency and strategies to improve light absorption in the photodetectors should be explored. Encapsulation techniques to prevent degradation of air-sensitive bP ink with oxides, 2D materials, and organics can prove to be useful as well (*40*, *41*). The future topics should be valuable given the tremendous potential of bP to serve as the leading candidate for next-generation MWIR electronics.

MATERIALS AND METHODS

Formulation of bP ink and spin-coating process

A schematic of the ink formulation process is shown in fig. S1. First, the bP (Smart Elements) crystal was crushed in a mortar and pestle into a powder form, of which around 5 to 20 mg was added to a glass

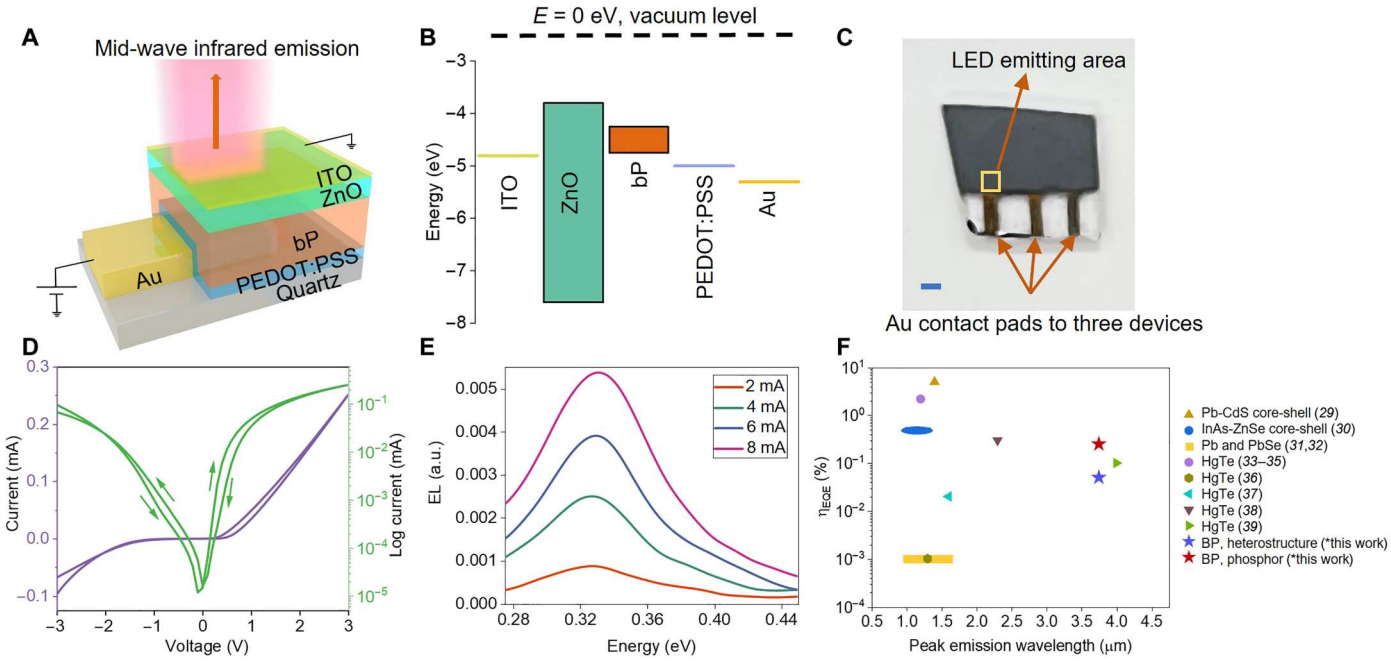

Fig. 4. LED based on heterostructure with bP ink. (**A**) Schematic showing the top-emitting LED cross section. (**B**) Energy band diagram showing electron and hole transport. (**C**) Photograph of the chip containing three devices. Scale bar, 1 mm. The device emitting area (~1 mm by 1 mm) is marked with a yellow boundary line and located in the area where the bottom gold electrode overlaps with the bP film. (**D**) *I-V* characteristics of the device. (**E**) EL from the device at a peak emission of 0.33 eV at injection currents of 2, 4, 6, and 8 mA. (**F**) External quantum efficiency (η_{EQE}) of the MWIR emitting bP heterostructure and bP-phosphor LED benchmarked against state-of-the-art QD-LEDs.

vial along with anhydrous NMP (1.5 ml). The solution was ultrasonicated with the 150-W Cole Parmer Ultrasonic Processor for a total duration of 30 min at a 60% amplitude and 50% duty cycle. The solution was then subjected to centrifugation at a speed of 8000 rpm for 30 min in 5-ml-sized plastic vials. The supernatant was removed, and 2.5 ml of toluene was added to the vial. An important note here is that not all the supernatant is removed. A few microliters of bP in NMP is left intentionally to improve the dispersibility of bP in the final solution. Removal of most of supernatant revealed that the bP particles start crashing in toluene. Following addition of 0.25 ml of toluene, 150 μl of oleyl amine (Sigma-Aldrich) was added to the same vial and then bath-sonicated for 30 s. This solution was again centrifuged at a speed of 8000 rpm for 3 min, and, then, the supernatant was removed to add 0.25 ml of toluene. This was followed by final bath sonication of the ink for 30 s, and, then, the ink was ready to be spin-coated. The bP flake thickness in the ink ranges between 5 and 150 nm with a lateral area of less than 1.5 μm^2, as shown in fig. S2. Quartz substrates sized ~5 mm by 5 mm were manually cut using a scriber and precleaned using deionized water, acetone, and isopropyl alcohol (IPA) before the spin coating. Ink was then spin-coated on the chip at a constant speed of 300 rpm and was allowed to dry for 1 to 5 min at room temperature. The slow speed during the spin coating enabled for the solution to stay on the chip.

PL and EL characterization

A laser diode with an emitting wavelength of 638 nm (Thorlabs) was used as the excitation source for the PL measurements, which was controlled by a laser diode controller (LDC500, Thorlabs). Voltage generated by a function generator (Agilent 81150) at a frequency of 5 kHz and 50% duty cycle was sent to the laser diode controller to modulate the excitation light. The light from the laser was then reflected by a mirror installed at the obscured center of the reflective objective and focused onto the sample. The light from the sample was directed to a Fourier transform infrared (FTIR) spectrometer (iS50, Thermo Fisher Scientific) through the 15× reflective objective. A HgCdTe (MCT) detector (liquid N_2–cooled) was used to detect the infrared signals together with a beam splitter of CaF_2. The signal from the detector was then locked-in using a lock-in amplifier (SR865, Stanford Research Systems) at the modulation frequency of the excitation laser. The output signal from the lock-in amplifier (separated signal from the thermal background) was then sent to a low-noise voltage preamplifier (SR560, Stanford Research Systems) and then lastly to the oscilloscope. Thereafter, the data were acquired from the oscilloscope and processed using fast Fourier transform in a custom-built LabView program. In the program, the raw signal as an interferogram in the time domain was converted to the frequency domain to collect the spectrally resolved PL.

For EL, same process was carried out, with the difference that instead of the red excitation laser. To modulate the EL device, a voltage-controlled current source (CS580, Stanford Research Systems), which was modulated by the function generator, was used to inject the current into the device. For the EL measurements, devices were wire-bonded in a 24-pin chip carrier in a Janis cryostat evacuated to a base pressure < 10^{-2} torr.

Further details on the measurement and calibration of output power can be found in our previously published work (*6*, *7*). The absorption of the bP ink film at around the laser excitation wavelength of 638 nm was measured to be 80%. The internal quantum

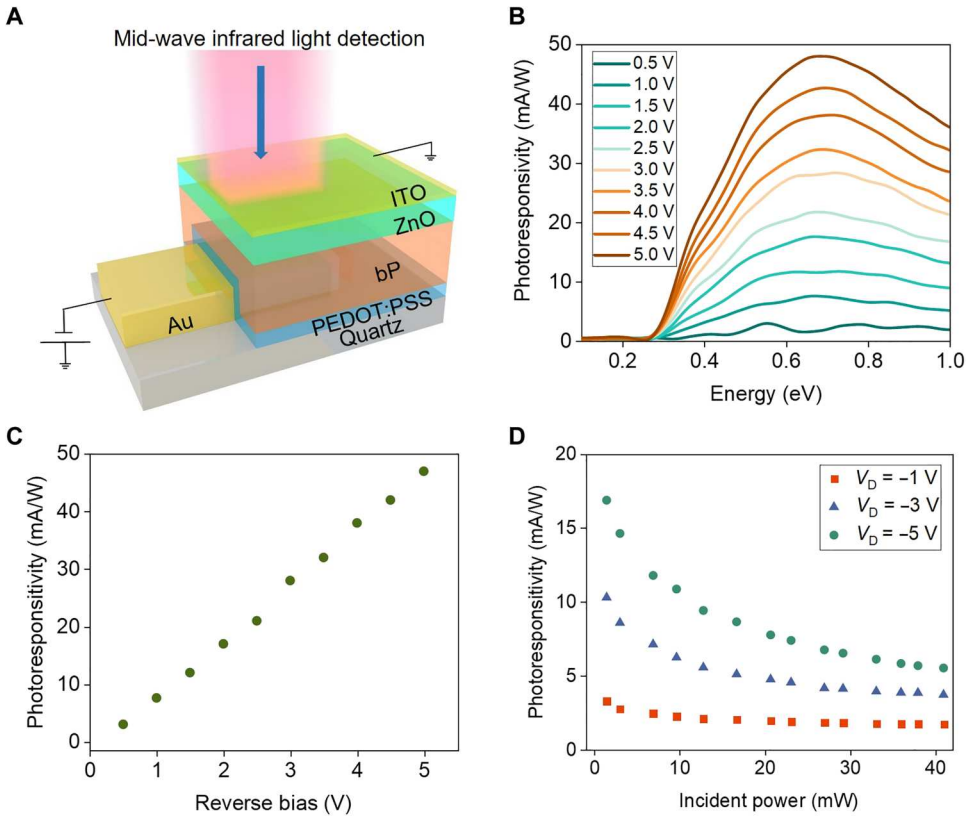

Fig. 5. BP ink–based photodetector. (**A**) Schematic showing the photodetector device cross section. (**B**) Spectrally resolved photo response of the devices to infrared light at different reverse biases. (**C**) Peak photoresponsivity as a function of reverse bias. (**D**) Photoresponsivity as a function of incident light power (λ = 638 nm) measured at different reverse biases.

yield (η_{QY}) was calculated using the external quantum yield (ratio of the detected photons to generated carriers) and the $4n^2$ light trapping factor (*42*). The red LED used for bP-phosphor experiment in Fig. 3 was purchased from Digikey (Luminus SST-20-DR Gen 2).

Device fabrication

The devices were made on quartz substrates sized ~5 mm by 5 mm, which were first cleaned with water, acetone, and IPA. Ti (10 nm) and Au (100 nm) were evaporated on the chip for electrodes and patterned on the chip using shadow masking. The spin-coating process of PEDOT:PSS (Clevios P VP AI 4083) was a two-step one, with 2500 rpm for the first 30 s and 4000 rpm for the next 1 min. It was seen that this process resulted in a thickness of 20 nm. The chip was then annealed at a temperature of 170°C for 15 min. Then, the bP ink was spin-coated at 300 rpm, and the chip was then annealed in a N_2-filled glove box at 100°C for 1 hour. Then, Kapton tape was used to mask the bottom Au electrodes. Subsequently, ~1 ml of ZnO (Sigma-Aldrich) was dynamically spin-coated on the chip at a speed of 2000 rpm, which resulted in a thickness of ~1.8 μm. Last, 20 nm of ITO was sputtered followed by removal of the tape.

Photodetector characterization

The photodetector measurements were done with the devices in a vacuumed chamber with the internal light source of the FTIR focused onto the emitting area with a 15× Schwarzschild objective. The photocurrent from the devices was inputted to a current amplifier (Stanford Research Systems), which also provided the bias voltage. The photodetector response at different light intensities was done using a red laser of 638 nm (Thorlabs), focused onto the device emitting area, and modulated at 5 kHz. The photocurrent from the device was directed to the current amplifier and locked-in at the laser frequency. The responsivity was calibrated using a National Institute of Standards and Technology (NIST) traceable Ge photodiode (Thorlabs) with known responsivity in place of the devices for all the measurements.

Supplementary Materials

This PDF file includes:

Supporting information S1 to S8
Figs. S1 to S7
References

REFERENCES AND NOTES

1. X. Li, Z. Yu, X. Xiong, T. Li, T. Gao, R. Wang, R. Huang, Y. Wu, High-speed black phosphorus field-effect transistors approaching ballistic limit. *Sci. Adv.* **5**, eaau3194 (2019).
2. C. Chen, F. Chen, X. Chen, B. Deng, B. Eng, D. Jung, Q. Guo, S. Yuan, K. Watanabe, T. Taniguchi, M. L. Lee, F. Xia, Bright mid-infrared photoluminescence from thin-film black phosphorus. *Nano Lett.* **19**, 1488–1493 (2019).
3. M. Amani, E. Regan, J. Bullock, G. H. Ahn, A. Javey, Mid-wave infrared photoconductors based on black phosphorus-arsenic alloys. *ACS Nano* **11**, 11724–11731 (2017).

4. Y. Chen, C. Tan, Z. Wang, J. Miao, X. Ge, T. Zhao, K. Liao, H. Ge, Y. Wang, F. Wang, Y. Zhou, P. Wang, X. Zhou, C. Shan, H. Peng, W. Hu, Momentum-matching and band-alignment van der Waals heterostructures for high-efficiency infrared photodetection. *Sci.Adv.* **8**, eabq1781 (2022).
5. J. Bullock, M. Amani, J. Cho, Y. Z. Chen, G. H. Ahn, V. Adinolfi, V. R. Shrestha, Y. Gao, K. B. Crozier, Y. L. Chueh, A. Javey, Polarization-resolved black phosphorus/molybdenum disulfide mid-wave infrared photodiodes with high detectivity at room temperature. *Nat. Photon.* **12**, 601–607 (2018).
6. H. Kim, S. Z. Uddin, D. H. Lien, M. Yeh, N. S. Azar, S. Balendhran, T. Kim, N. Gupta, Y. Rho, C. P. Grigoropoulos, K. B. Crozier, A. Javey, Actively variable-spectrum optoelectronics with black phosphorus. *Nature* **596**, 232–237 (2021).
7. N. Gupta, H. Kim, N. S. Azar, S. Z. Uddin, D. H. Lien, K. B. Crozier, A. Javey, Bright mid-wave infrared resonant-cavity light-emitting diodes based on black phosphorus. *Nano. Lett.* **22**, 1294–1301 (2022).
8. P. Bhaskar, A. W. Achtstein, M. J. Vermeulen, L. D. A. Siebbeles, Radiatively dominated charge carrier recombination in black phosphorus. *J. Phys. Chem. C* **120**, 13836–13842 (2016).
9. N. Higashitarumizu, S. Z. Uddin, D. Weinberg, N. S. Azar, I. K. M. Reaz Rahman, V. Wang, K. B. Crozier, E. Rabani, A. Javey, Anomalous thickness dependence of photoluminescence quantum yield in black phosphorous. *Nat. Nanotechnol.* **18**, 507–513 (2023).
10. D. Hanlon, C. Backes, E. Doherty, C. S. Cucinotta, N. C. Berner, C. Boland, K. Lee, A. Harvey, P. Lynch, Z. Gholamvand, S. Zhang, K. Wang, G. Moynihan, A. Pokle, Q. M. Ramasse, N. M. Evoy, W. J. Blau, J. Wang, G. Abellan, F. Hauke, A. Hirsch, S. Sanvito, D. D. O'Regan, G. S. Duesberg, V. Nicolosi, J. N. Colemana, Liquid exfoliation of solvent-stabilized few-layer black phosphorus for applications beyond electronics. *Nat. Commun.* **6**, 8563 (2015).
11. X. Gong, L. Guan, Q. Li, Y. Li, T. Zhang, H. Pan, Q. Sun, Y. Shen, C. Grätzel, S. M. Zakeeruddin, M. Grätzel, M. Wang, Black phosphorus quantum dots in inorganic perovskite thin films for efficient photovoltaic application. *Sci. Adv.* **6**, eaay5661 (2020).
12. S. Lin, S. Liu, Z. Yang, Y. Li, T. W. Ng, Z. Xu, Q. Bao, J. Hao, C. S. Lee, C. Surya, F. Yan, S. P. Lau, Solution-processable ultrathin black phosphorus as an effective electron transport layer in organic photovoltaics. *Adv. Funct. Mater.* **26**, 864–871 (2016).
13. S. Pinilla, J. Coelho, K. Li, J. Liu, V. Nicolosi, Two-dimensional material inks. *Nat. Rev. Mater.* **7**, 717–735 (2022).
14. G. Hu, T. Albrow-Owen, X. Jin, A. Ali, Y. Hu, R. C. T. Howe, K. Shehzad, Z. Yang, X. Zhu, R. I. Woodward, T.-C. Wu, H. Jussila, J.-B. Wu, P. Peng, P.-H. Tan, Z. Sun, E. J. R. Kelleher, M. Zhang, Y. Xu, T. Hasan, Black phosphorus ink formulation for inkjet printing of optoelectronics and photonics. *Nat. Commun.* **8**, 278 (2017).
15. H. Y. Jun, S. O. Ryu, S. H. Kim, J. Y. Kim, C. H. Chang, S. O. Ryu, C. H. Choi, Inkjet printing of few-layer enriched black phosphorus nanosheets for electronic devices. *Adv. Electron. Mater.* **7**, 2100577 (2021).
16. J. N. Coleman, M. Lotya, A. O'Neill, S. D. Bergin, P. J. King, U. Khan, K. Young, A. Gaucher, S. de, R. J. Smith, I. V. Shvets, S. K. Arora, G. Stanton, H. Y. Kim, K. Lee, G. T. Kim, G. S. Duesberg, T. Hallam, J. J. Boland, J. J. Wang, J. F. Donegan, J. C. Grunlan, G. Moriarty, A. Shmeliov, R. J. Nicholls, J. M. Perkins, E. M. Grieveson, K. Theuwissen, D. W. McComb, P. D. Nellist, V. Nicolosi, Two-dimensional nanosheets produced by liquid exfoliation of layered materials. *Science* **331**, 568–571 (2011).
17. S. Mourdikoudis, L. M. Liz-Marzán, Oleylamine in nanoparticle synthesis. *Chem. Mater.* **25**, 1465–1476 (2013).
18. A. Favron, E. Gaufrès, F. Fossard, A. L. Phaneuf-L'Heureux, N. Y. W. Tang, P. L. Lévesque, A. Loiseau, R. Leonelli, S. Francoeur, R. Martel, Photooxidation and quantum confinement effects in exfoliated black phosphorus. *Nat. Mater.* **14**, 826–832 (2015).
19. Y. P. Varshni, "Band-to-band radiative recombination in groups IV, VI, and III-V semiconductors (I)" in *Physica Status Solidi* (De Gruyter), (2022), chap 2.
20. K. L. Vodopyanov, H. Graener, C. C. Phillips, T. J. Tate, Picosecond carrier dynamics and studies of Auger recombination processes in indium arsenide at room temperature. *Phys. Rev. B Condens. Matter.* **46**, 13194–13200 (1992).
21. A. Rogalski, K. Jóźwikowski, The intrinsic carrier concentration in $Pb_{1-x}Sn_xTe$, $Pb_{1-x}Sn_xSe$, and $PbS_{1-x}Se_x$. *Phys. Status Solidi A* **111**, 559–565 (1989).
22. R. Klann, T. Höfer, R. Buhleier, T. Elsaesser, J. W. Tomm, Fast recombination processes in lead chalcogenide semiconductors studied via transient optical nonlinearities. *J. Appl. Phys.* **77**, 277–286 (1995).
23. S. Marchetti, M. Martinelli, R. Simili, The Auger recombination coefficient in InAs and GaSb derived from the infrared dynamical plasma reflectivity. *J. Phys. Condens. Matter* **14**, 3653–3656 (2002).
24. E. Kioupakis, P. Rinke, K. T. Delaney, C. G. Van de Walle, Indirect Auger recombination as a cause of efficiency droop in nitride light-emitting diodes. *Appl. Phys. Lett.* **98**, 161107 (2011).
25. H. Guo, Y. Chen, M. B. Cortie, X. Liu, Q. Xie, X. Wang, D. L. Peng, Shape-selective formation of monodisperse copper nanospheres and nanocubes via disproportionation reaction route and their optical properties. *J. Phys. Chem. C* **118**, 9801–9808 (2014).
26. X. Dai, Z. Zhang, Y. Jin, Y. Niu, H. Cao, X. Liang, L. Chen, J. Wang, X. Peng, Solution-processed, high-performance light-emitting diodes based on quantum dots. *Nature* **515**, 96–99 (2014).
27. X. Zong, H. Hu, G. Ouyang, J. Wang, R. Shi, L. Zhang, Q. Zeng, C. Zhu, S. Chen, C. Cheng, B. Wang, H. Zhang, Z. Liu, W. Huang, T. Wang, L. Wang, X. Chen, Black phosphorus-based van der Waals heterostructures for mid-infrared light-emission applications. *Light. Sci. Appl.* **9**, 114 (2020).
28. W. M. H. Sachtler, G. J. H. Dorgelo, A. A. Holscher, The work function of gold. *Surf. Sci.* **5**, 221–229 (1966).
29. G. J. Supran, K. W. Song, G. W. Hwang, R. E. Correa, J. Scherer, E. A. Dauler, Y. Shirasaki, M. G. Bawendi, V. Bulović, High-performance shortwave-infrared light-emitting devices using core–shell (PbS–CdS) colloidal quantum dots. *Adv. Mater.* **27**, 1437–1442 (2015).
30. N. Tessler, V. Medvedev, M. Kazes, S. H. Kan, U. Banin, Efficient near-infrared polymer nanocrystal light-emitting diodes. *Science* **295**, 1506–1508 (2002).
31. L. Bakueva, S. Musikhin, M. A. Hines, T.-W. F. Chang, M. Tzolov, G. D. Scholes, E. H. Sargent, Size-tunable infrared (1000–1600 nm) electroluminescence from Pbs quantum-dot nanocrystals in a semiconducting polymer. *Appl. Phys. Lett.* **82**, 2895–2897, 2897 (2003).
32. J. S. Steckel, S. Coe-Sullivan, V. Bulović, M. G. Bawendi, 1.3 μm to 1.55 μm tunable electroluminescence from PbSe quantum dots embedded within an organic device. *Adv. Mater.* **15**, 1862–1866 (2003).
33. J. Qu, P. Rastogi, C. Gréboval, D. Lagarde, A. Chu, C. Dabard, A. Khalili, H. Cruguel, C. Robert, X. Z. Xu, S. Ithurria, M. G. Silly, S. Ferré, X. Marie, E. Lhuillier, Electroluminescence from HgTe nanocrystals and its use for active imaging. *Nano Lett.* **20**, 6185–6190 (2020).
34. Y. Prado, J. Qu, C. Gréboval, C. Dabard, P. Rastogi, A. Chu, A. Khalili, X. Z. Xu, C. Delerue, S. Ithurria, E. Lhuillier, Seeded growth of HgTe nanocrystals for shape control and their use in narrow infrared electroluminescence. *Chem. Mater.* **33**, 2054–2061 (2021).
35. E. Bossavit, J. Qu, C. Abadie, C. Dabard, T. Dang, E. Izquierdo, A. Khalili, C. Gréboval, A. Chu, S. Pierini, M. Cavallo, Y. Prado, V. Parahyba, X. Z. Xu, A. Decamps-Mandine, M. Silly, S. Ithurria, E. Lhuillier, Optimized infrared LED and its use in an all-HgTe nanocrystal-based active imaging setup. *Adv. Opt. Mater.* **10**, 2101755 (2022).
36. D. S. Koktysh, N. Gaponik, M. Reufer, J. Crewett, U. Scherf, A. Eychmüller, J. M. Lupton, A. L. Rogach, J. Feldmann, Near-infrared electroluminescence from HgTe nanocrystals. *ChemPhysChem* **5**, 1435–1438 (2004).
37. É. O'Connor, A. O'Riordan, H. Doyle, S. Moynihan, A. Cuddihy, G. Redmond, Near-infrared electroluminescent devices based on colloidal HgTe quantum dot arrays. *Appl. Phys. Lett.* **86**, 201114 (2005).
38. J. Qu, M. Weis, E. Izquierdo, S. G. Mizrahi, A. Chu, C. Dabard, C. Gréboval, E. Bossavit, Y. Prado, E. Péronne, S. Ithurria, G. Patriarche, M. G. Silly, G. Vincent, D. Boschetto, E. Lhuillier, Electroluminescence from nanocrystals above 2 μm. *Nat. Photonics* **16**, 38–44 (2022).
39. X. Shen, J. C. Peterson, P. Guyot-Sionnest, Mid-infrared HgTe colloidal quantum dot LEDs. *ACS Nano* **16**, 7301–7308 (2022).
40. Y. Abate, D. Akinwande, S. Gamage, H. Wang, M. Snure, N. Poudel, S. B. Cronin, Recent progress on stability and passivation of black phosphorus. *Adv. Mater.* **30**, e1704749 (2018).
41. J. D. Wood, S. A. Wells, D. Jariwala, K. S. Chen, E. K. Cho, V. K. Sangwan, X. Liu, L. J. Lauhon, T. J. Marks, M. C. Hersam, Effective passivation of exfoliated black phosphorus transistors against ambient degradation. *Nano Lett.* **14**, 6964–6970 (2014).
42. E. Yablonovitch, O. Miller, *The Influence of the 4n2 Light Trapping Factor on Ultimate Solar Cell Efficiency* (Optica Publishing Group, (2010).
43. C. W. Chen, S. Y. Hsiao, C. Y. Chen, H. W. Kang, Z. Y. Huang, H. W. Lin, Optical properties of organometal halide perovskite thin films and general device structure design rules for perovskite single and tandem solar cells. *J. Mater. Chem. A* **3**, 9152–9159 (2015).
44. W. L. Bond, Measurement of the refractive indices of several crystals. *J. Appl. Phys.* **36**, 1674–1677 (1965).

Acknowledgments: N.G. thanks H. Kim and Y. Zhao for fruitful discussions. N.H. acknowledges support from the Postdoctoral Fellowships for Research Abroad of Japan Society for the Promotion of Science. We thank G. Cho and J. Park for inputs on the ink formation process. Device fabrication was supported by Berkeley Sensor & Actuator Center. **Funding:** This work was funded by the U.S. Department of Energy, Office of Science, Office of Basic Energy Sciences, Materials Sciences and Engineering Division under contract DE-AC02-05-CH11231 (EMAT program KC1201). **Author contributions:** A.J. and N.G. conceived the idea for the project and designed the experiments. N.G. and S.W. formulated the ink process and carried out the fabrication and measurements of devices. S.W., N.H., and V.W. performed the optical simulations and efficiency calculations. S.W. performed the SEM characterizations. N.H. performed the Raman characterization. K.L. and C.P. helped with the measurements. N.G., S.W.,

N.H., and A.J. wrote the manuscript. All authors discussed the results and authored the paper. **Competing interests:** The authors declare that they have no competing interests. **Data and materials availability:** All data needed to evaluate the conclusions in the paper are present in the paper and/or the Supplementary Materials.

Submitted 30 May 2023
Accepted 9 November 2023
Published 8 December 2023
10.1126/sciadv.adi9384